Materials Advances

ROYAL SOCIETY OF CHEMISTRY

PAPER

Cite this: DOI: 10.1039/d5ma01435b

Solution-processed La-substituted $Ba_2Bi_2O_6$ photocathodes with enhanced photoelectrochemical activity: a combined experimental and computational study

Bradley Francis Lewis, [a] Giuseppe Mallia, [b] Tianhao Lan, [c] Evan Tillotson, [de] Minzhi Chen, [a] Hongbo Zhang, [a] Jamie Southouse, [f] Sarah J. Haigh, [de] Nicholas M. Harrison, [b] Ji-Seon Kim [cgh] and Salvador Eslava *[a]

In the search for solution-processed p-type semiconductors for photocathodic hydrogen evolution, we have developed a spin-coating method for fabricating the double perovskite $Ba_2Bi_2O_6$ using polyvinylpyrrolidone as a polymer template and a sol–gel mixture of barium and bismuth acetates. This method produces films with high porosity and well-defined grain boundaries, enlarging semiconductor/electrolyte interfacial area. Photocurrent responses are activated by 20% atomic substitution of Bi by La in $Ba_2Bi_2O_6$ (*i.e.* $Ba_2Bi_{1.6}La_{0.4}O_6$), achieving a photocurrent density of -0.85 mA cm^{-2} at +0.68 V_{RHE} under simulated sunlight conditions. However, this high photocurrent is not accompanied by hydrogen evolution and is attributed instead to the reduction of bismuth through its oxidation states. Tauc plot analyses of incident photon-to-current efficiencies reveal a bandgap reduction from 2.70 to 2.53 eV with an optimal amount of La substitution, supporting the observed improvement in light absorption and photocurrent. Mott–Schottky plots show a clear slope for $Ba_2Bi_{1.6}La_{0.4}O_6$, while $Ba_2Bi_2O_6$ exhibited a flat response, indicating poor conductivity in $Ba_2Bi_2O_6$ that was only activated by La substitution. Williamson–Hall analysis of X-ray diffraction reveals that La substitution doubles the microstrain, while scanning transmission electron microscopy confirms the uniform elemental composition and excellent crystallinity of the La-substituted films. Computational analysis supports the experimental results, showing that La substitution increases the lattice parameters, induces microstrain, and reduces the bandgap. These findings demonstrate a solution-based approach for preparing $Ba_2Bi_2O_6$ double perovskite photocathodes and show how La substitution enhances photocurrent performance. They also highlight the remaining challenge of directing these photocurrents toward improved photoelectrochemical hydrogen evolution.

Received 9th December 2025,
Accepted 4th May 2026

DOI: 10.1039/d5ma01435b

rsc.li/materials-advances

Introduction

The global energy crisis presents a significant challenge in meeting rising energy demands while heavily relying on limited fossil fuel reserves, contributing to environmental damage and climate change.[1–3] This situation highlights the urgent need to transition toward sustainable and renewable energy sources to ensure long-term energy security and reduce the harmful effects of carbon emissions.[4–6] Photoelectrochemical (PEC) water splitting emerges as a promising solution to this crisis by using solar energy to convert water into hydrogen and oxygen.[7–9] In the PEC process, semiconductor materials are incorporated in electrodes of electrochemical cells to form photocathodes and photoanodes that can absorb solar photons to generate electron–hole pairs and enable the reduction of water to hydrogen and the simultaneous oxidation of water to produce oxygen.[10] Since hydrogen is a clean, high-energy fuel, its production through PEC water splitting offers a renewable and carbon-neutral alternative to fossil fuels, helping to decrease greenhouse gas emissions and mitigate the energy crisis.[11,12]

Relative to the breadth of literature on photoanodes for the oxygen evolution reaction (OER), that on photocathode

[a] Department of Chemical Engineering and Centre for Processable Electronics, Imperial College London, London, SW7 2AZ, UK. E-mail: s.eslava@imperial.ac.uk
[b] Department of Chemistry, Imperial College London, London, W12 0BZ, UK
[c] Department of Physics and Centre for Processable Electronics, Imperial College London, London, SW7 2AZ, UK
[d] Department of Materials, University of Manchester, Manchester, M13 9PL, UK
[e] National Graphene Institute, University of Manchester, Manchester, M13 9PL, UK
[f] BP Innovation & Engineering, Applied Sciences, BP plc, Saltend, Hull, HU12 8DS, UK
[g] Department of Chemistry, University of Oxford, South Parks Road, Oxford, OX1 3QZ, UK
[h] Department of Physics, Ewha Womans University, Seoul, 03760, Republic of Korea

development for the hydrogen evolution reaction (HER) is limited. Photocathode material identification, optimisation and development are critical to the success of overall PEC water splitting.[13,14] Metal oxides, in particular ternary metal oxides, have been identified as a promising class of materials for this application owing to their excellent stability in air, water and light.[15–17] However, these materials pose significant challenges due to their inherent characteristics, notably, short diffusion lengths of photogenerated charge carriers and poor light absorption.[18–21] Improving their light absorption properties, as well as their solid–electrolyte surface interactions, is required to unlock ternary metal oxide's full potential as photocathode materials.

Double perovskites, $A_2B_2O_6$, which have units cells consisting of double the typical perovskite ABO_3 unit, receive wide attention in catalysis and other fields.[22] Substitution of the B-site cation offers regulation of the Fermi energy level (E_F) by adapting the d-band centre,[22] which in turn, controls the p- or n-type nature of the semiconductor. Furthermore, doping or substitution of the B-site of double perovskites is reported to facilitate the movement of electrons through oxygen vacancies.[23] Guo *et al.* adopted this approach by partially incorporating La^{3+} into the B-site of $Ba_2Bi_2O_6$, on Au substrates, resulting in high photocathodic PEC current density, although hydrogen evolution was not confirmed.[24] Further studies on $Ba_2Bi_2O_6$ remain limited, particularly in the context of PEC water splitting. Among the few reports available, the fabrication procedures are often complex, costly,[25] or primarily focused on photoanode development for solar OER.[26] Despite this, $Ba_2Bi_2O_6$ exhibits inherently promising characteristics, including p-type tunability through doping, rendering it a strong candidate for the development of novel photocathodes.

In the search to develop $Ba_2Bi_2O_6$ films, this article presents an inexpensive polymer-templated spin-coating deposition on fluorine-doped coated glass substrates and studies the partial substitution of Bi by La, reaching best results for $Ba_2Bi_{1.6}La_{0.4}O_6$ (20 at% La). Scanning electron micrographs illustrate the benefit of using the polymer template for improving uniformity whilst maintaining good levels of porosity to maximize semiconductor/electrolyte interactions. X-ray diffraction (XRD) of $Ba_2Bi_{1.6}La_{0.4}O_6$ and $Ba_2Bi_2O_6$ films confirm that both are highly crystalline, and Williamson–Hall plots determine that La substitution doubles microstrain, aiding in charge transport according to Mott–Schottky analysis of impedance results. Moreover, computational results confirm that the extra strain is induced by partial substitution of Bi by La, contributing to reducing the bandgap of the material as the lattice parameters increase due to unit cell expansion. All photocathodes show dark current and photocurrents under light illumination. La-substituted samples show the strongest photocurrent responses, providing $Ba_2Bi_{1.6}La_{0.4}O_6$ a high current density of -0.85 mA cm^{-2} at +0.67 V *vs.* the reversible hydrogen electrode (V_{RHE}). However, these currents and photocurrents are transient and not accompanied by hydrogen detection, therefore they are assigned to bismuth reduction through its oxidation states. These findings uncover opportunities to achieve high photocurrents with these materials but also challenges in their application for PEC water splitting.

Experimental section

Film fabrication

$Ba_2Bi_2O_6$ thin films with various levels of La substitution for Bi were prepared by spin-coating precursor solution containing a sacrificial polymer template on top of fluorine-doped tin oxide coated aluminoborosilicate glass (FTO–glass) from Solaronix, Switzerland. The FTO–glass substrates were first cleaned under ultrasonication in 5% Hellmanex III detergent aqueous solution, acetone, and 2-propanol sequentially for 10 min each, and subsequently UV–ozone treated for 20 min. A precursor solution was stirred for 1 h consisting of 0.05 mmol $Ba(CH_3COO)_2$, $(0.05–x)$ mmol $Bi(CH_3COO)_2$ and x mmol $La(CH_3COO)_2$ dissolved in 0.25 ml acetic acid and 1 ml of double deionised water, intentionally decreasing Bi content whilst adding La to promote substitution of the B-site. The values of x were 0, 0.0025 (5 at%), 0.005 (10 at%) and 0.01 (20 at%). The overall concentration of the sol–gel was maintained for all samples. Once fully combined, 0.1 g polyvinylpyrrolidone (10% w/v) was added, and the mixture was stirred for a further 1 h. Subsequently, 60 μL of this fully homogenous solution was spin-coated onto a cleaned FTO-coated glass at 2000 rpm for 30 s with acceleration 100 rpm s^{-1}. The spin-coated thin film was then heated in air at a rate of 3.8 °C min^{-1} up to a temperature of 700 °C and kept for 1 h to produce a one-layer film with the nominal formula $Ba_2Bi_{2-x}La_xO_6$ (x = 0, 0.1, 0.2, 0.4).

PEC measurements

PEC measurements were conducted on a three-electrode electrochemical cell including a working electrode, an Ag/AgCl reference electrode, a Pt counter electrode, and 0.1 M Na_2SO_4 electrolyte at pH 12, adjusted with NaOH pellets. A xenon lamp (300 W) assembled with an AM 1.5G solar simulator filter from Quantum Design was employed as the simulated sunlight source. The intensity determined at the position of the working electrode was 100 mW cm^{-2} (1 sun). In addition to chopped illumination, the external potential was also varied in the measurement process, swept linearly from +1.4 to 0.2 V_{RHE} at a scan rate of 10 mV s^{-1}. IPCE measurements were recorded at +1.05 V_{RHE} from 300 to 700 nm. Electrochemical impedance spectroscopy (EIS) measurements were conducted at various potentials in the absence of light to generate a Mott–Schottky plot. These measurements were performed at constant frequencies of 1, 3, and 5 kHz, and represented considering the following equation:

$$\frac{1}{C^2} = \frac{2}{A^2 N_D e \varepsilon \varepsilon_0}\left(V - V_{fb} - \frac{K_b T}{e}\right) \quad (1)$$

e elemental charge, ε_0 is the permittivity of the vacuum, ε is the relative permittivity of $Ba_2Bi_2O_6$ (30), V is the applied potential, V_{fb} is the flat band potential, K_b is the Boltzmann constant,

and T is the temperature. The hole-carrier density was then determined from these plots using the following equation:

$$N_D = \left(\frac{2}{A^2 e\varepsilon\varepsilon_0}\right)\left(\frac{d\left(\frac{1}{C^2}\right)}{d(V)}\right)^{-1} \quad (2)$$

Field emission-scanning electron microscopy (FE-SEM) micrographs were obtained using a ZEISS LEO 1525 FE-SEM. Cross-sectional samples of the $Ba_2Bi_{1.6}La_{0.4}O_6$ thin films were prepared using a dual-beam focused ion beam scanning electron microscope (FIB-SEM), Zeiss Crossbeam 540. Prior to ion-beam milling, a protective Pt layer was deposited on the film surface to minimise ion-beam damage during FIB sample preparation, initially laying down Pt with electron-beam deposition before increasing the thickness with ion-beam deposition. Cross sectional lamellae were subsequently lifted out from the substrate using a micromanipulator and attached to a TEM grid using Pt deposition. Finally, the lamellae were thinned to electron transparency using ion-beam currents starting from 300 pA and reducing to 5 pA for final polishing. High-angle annular dark field (HAADF) STEM imaging was performed on an aberration-corrected ThermoFisher Titan STEM (G2 80-200), operating with a probe convergence angle of 21 mrad, an acceleration voltage of 200 kV, a probe current of 60 pA and inner/outer collection angles of 68–200 mrad for the HAADF detector. STEM energy dispersive X-ray spectroscopy (EDS) revealed the elemental distributions (Ba, Bi, La, O) across the cross section of the film. Image processing and presentation were carried out using Adobe Illustrator.

The XRD patterns were obtained over the 2θ range of 18°–80° in steps of 0.008° and subsequently analyzed using the HighScore software. X-ray photoelectron spectroscopy (XPS) spectra were acquired using ThermoFisher K-Alpha+ using a monochromated Al Kα X-ray source. Binding energies were referenced relative to adventitious carbon at 284.8 eV. XPS data were processed using Avantage. The Fermi level of the samples was determined using a Kelvin probe system with a vibrating gold tip (d = 2 mm) under controlled temperature and humidity conditions. The work function was calculated from the contact potential difference (CPD) between the sample and the tip, calibrated by using a freshly cleaned silver reference. In the dark, the Fermi energy was assumed to be equal to the work function (WF).

The Kelvin probe was also used to measure surface photovoltage (SPV), which is the change of surface potential induced by illumination. The standard SPV measurement in this project was as follows: first, the WF was measured in the dark for 20 s, then a white light with an intensity of approximately 0.28 sun was turned on for 100 s to generate SPV on the upper surface of the sample three times, each followed by measuring in the dark for 150 s to observe the SPV transient decay. Prior to SPV measurement, work function was confirmed to reach steady state.

The valence band maximum (VBM) was measured by ambient photoemission spectroscopy (APS). In this measurement, a Kelvin probe was employed to detect the current produced by the electrons ejected from sample surfaces and atmospheric ions reaching the tip at ambient pressure under UV illumination, the data for which include the initial photoelectric threshold. These anions collected by a biased tip generate a photocurrent proportional to the density of ionized electrons. Since the photoemission from binding energies below the VBM value can be attributed to the presence of defect/trap states, the integrated area below the photoemission threshold can be used to compare trap state densities of different materials in a quantitative way. The WF, APS, and SPV measurements were performed in an APS04 system (KP Technology).

The crystal structures of the photocathodes were investigated by XRD using a PANalytical X'Pert diffractometer (Cu Ka, λ = 1.54 Å) at 40 kV and 40 mA. Further analysis of the diffractograms was carried out employing the Williamson–Hall plots described in eqn (3).

$$\beta\cos\theta = 4\varepsilon\sin\theta + \frac{K\lambda}{D} \quad (3)$$

where β is the full width at half maximum, θ is Bragg's angle, λ is the wavelength of radiation, K is shape factor and constant bearing value (0.98), D is crystallite size, and ε is microstrain.

Results and discussion

A straightforward fabrication method was developed to spin-coat $Ba_2Bi_2O_6$ precursor onto FTO-glass substrates incorporating a polymer template within a sol–gel mixture. The sol–gel mixture consists of Ba, Bi and La acetates, fully homogenised in a solvent mixture of water and acetic acid, as well as polymer polyvinylpyrrolidone (PVP). After stirring, each of the sol–gel/polymer solutions were spin-coated on FTO-glass substrates and then annealed at 700 °C to obtain thin films with the nominal formulas $Ba_2Bi_2O_6$, $Ba_2Bi_{1.9}La_{0.1}O_6$, $Ba_2Bi_{1.8}La_{0.2}O_6$ and $Ba_2Bi_{1.6}La_{0.4}O_6$. The use of high-temperature resistant aluminoborosilicate glass ensured conservation of the FTO properties after annealing. Higher La concentrations above 20 at% were not possible due to the solubility limit of La acetate in the solvent mixture. All the films were visually uniform, free of coating defects such as comets or striations and of black mirror-like appearance.

Their PEC responses (current density *vs.* potential) were collected under chopped simulated sunlight at 1 sun using a three-electrode system with a 0.1 M Na_2SO_4 electrolyte at pH 12 (Fig. 1a). The $Ba_2Bi_2O_6$ photocathode shows small photocurrent above +0.9 V_{RHE}, whilst all the La-substituted films show substantial photocurrent above this potential ($\sim$100–300 μA cm^{-2}). Baselined photocurrent densities at +0.65–0.69 V_{RHE} do not show a clear trend of increasing photocurrent density with the La substitution, but it is clear that La increases photocurrents and the best performing film is achieved with 20 at% La composition, $Ba_2Bi_{1.6}La_{0.4}O_6$, achieving a maximum photocurrent density of −0.85 mA cm^{-2} at +0.68 V_{RHE} (Fig. 1b). The PEC

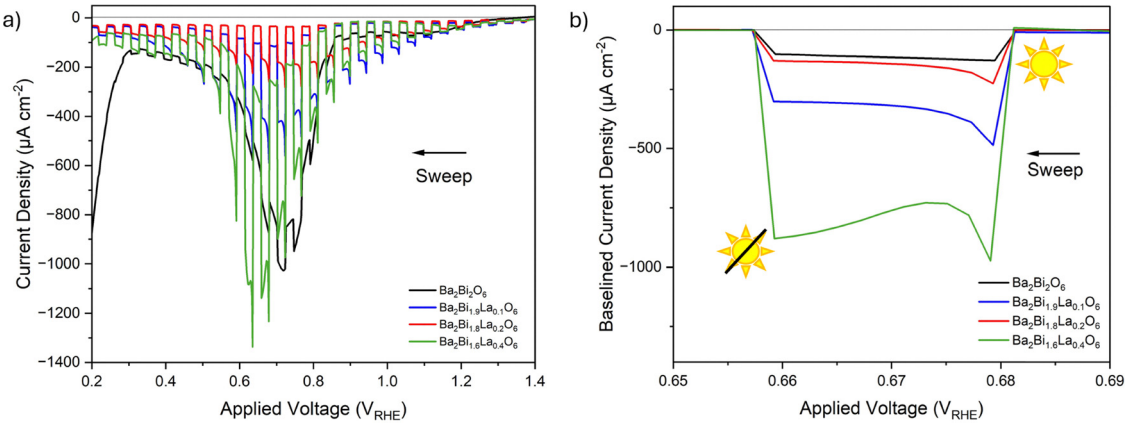

Fig. 1 (a) Current–potential curves for $Ba_2Bi_2O_6$ films with various levels of La substitution in the Bi sites, measured under chopped simulated sunlight (AM1.5G, 100 mW cm^{-2}) in pH 12 0.1 M Na_2SO_4. Linear sweep from +1.4 to +0.2 V_{RHE} at 10 mV s^{-1}. (b) Baselined current–potential measurements from +0.69 to +0.65 V_{RHE}.

response at potentials lower than +0.9 V_{RHE} shows a clear dark current present, again with no clear trend with the concentration of La. These dark currents and photocurrents were not accompanied by hydrogen gas detection in a gas chromatograph with barrier ionisation detector (GC-BID); therefore, they are assigned to the reduction of bismuth cycling through multiple oxidation states *i.e.* $Bi^{5+} \rightarrow Bi^{4+}$, $Bi^{5+} \rightarrow Bi^{3+}$, $Bi^{4+} \rightarrow Bi^{3+}$ at potentials shortly below +0.9 V_{RHE} and $Bi^{3+} \rightarrow Bi^{+}$ and $Bi^{3+} \rightarrow Bi$ at even lower potentials.[27,28] All the films showed decolouration during the experiments, further confirming oxidation state changes. Moreover, a second linear PEC scan shows a strong decay in current and photocurrent, supporting the assignment of the measured photocurrent to Bi redox rather than catalytic HER (Fig. S1).

The film with the best photocurrent performance, $Ba_2Bi_{1.6}La_{0.4}O_6$, was investigated with FE-SEM to probe the morphological effect of the addition of PVP polymer during synthesis. The plan view micrographs show that without the addition of PVP in the precursor sol–gel, the film illustrates poor surface coverage with visible signs of exposed FTO (Fig. 2a). This poor coverage agrees with its visual appearance as browner and dimmer in the absence of PVP, while the film has a black mirror-like appearance with PVP (Fig. S2). In contrast, the SEM of the film with the addition of 10% w/v PVP shows high coverage, as well as distinct grain boundaries and intergranular porosity (Fig. 2b), which increases the area of the semiconductor/electrolyte interface and explains the increased photocathodic currents (Fig. S3).[29] Cross-sectional FE-SEM shows that the polymer-templated film thickness is ~200 nm and confirms the uniform and porous morphology seen in plan-view FE-SEM.

XRD analysis shows excellent crystallinity for both $Ba_2Bi_{1.6}La_{0.4}O_6$ and $Ba_2Bi_2O_6$ films (Fig. 3a). The diffractograms show clear peaks associated to $Ba_2Bi_2O_6$ (JCPDS: 01-074-2124) and the FTO-glass substrate. The diffractions peaks associated with $Ba_2Bi_2O_6$ at 20.6°, 29.3°, 41.8°, 60.4° and 68.5° (2θ) correspond to (110), (200), (211), (220) and (310) planes, respectively, and have similar peak intensities for both materials suggesting that both films have similar orientations and textures. Furthermore, no shifts in peak positions are observed, suggesting that the partial La substitution, confirmed by XPS elemental analysis (Fig. S4 and Table S1), does not induce significant structural changes in the cubic double perovskite unit cell. The diffraction peaks attributed to bismuth subcarbonate (JCPDS: 41-1488) at 30.4 and 43.6° are observed exclusively in the $Ba_2Bi_2O_6$ sample,

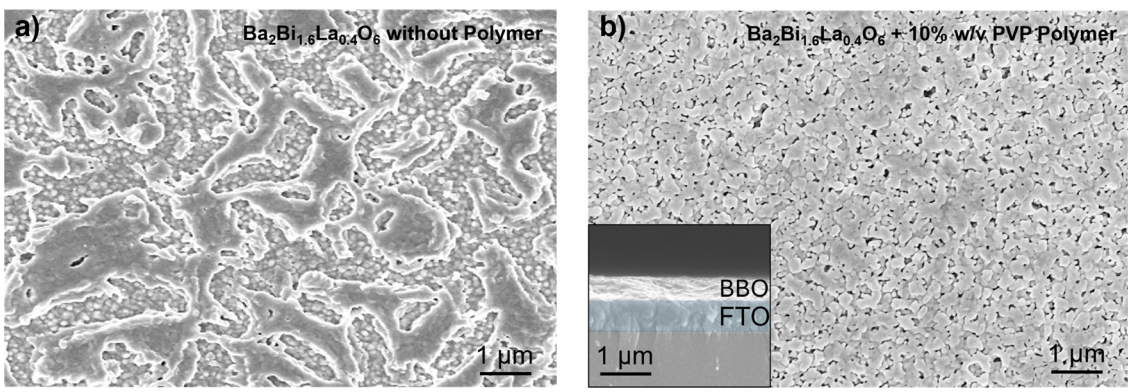

Fig. 2 FE-SEM top-view micrographs of the $Ba_2Bi_{1.6}La_{0.4}O_6$ films prepared (a) without and (b) with a 10% w/v PVP polymer template. (b insert) Cross-sectional FE-SEM micrograph of the $Ba_2Bi_{1.6}La_{0.4}O_6$ film prepared with a 10% w/v PVP polymer template.

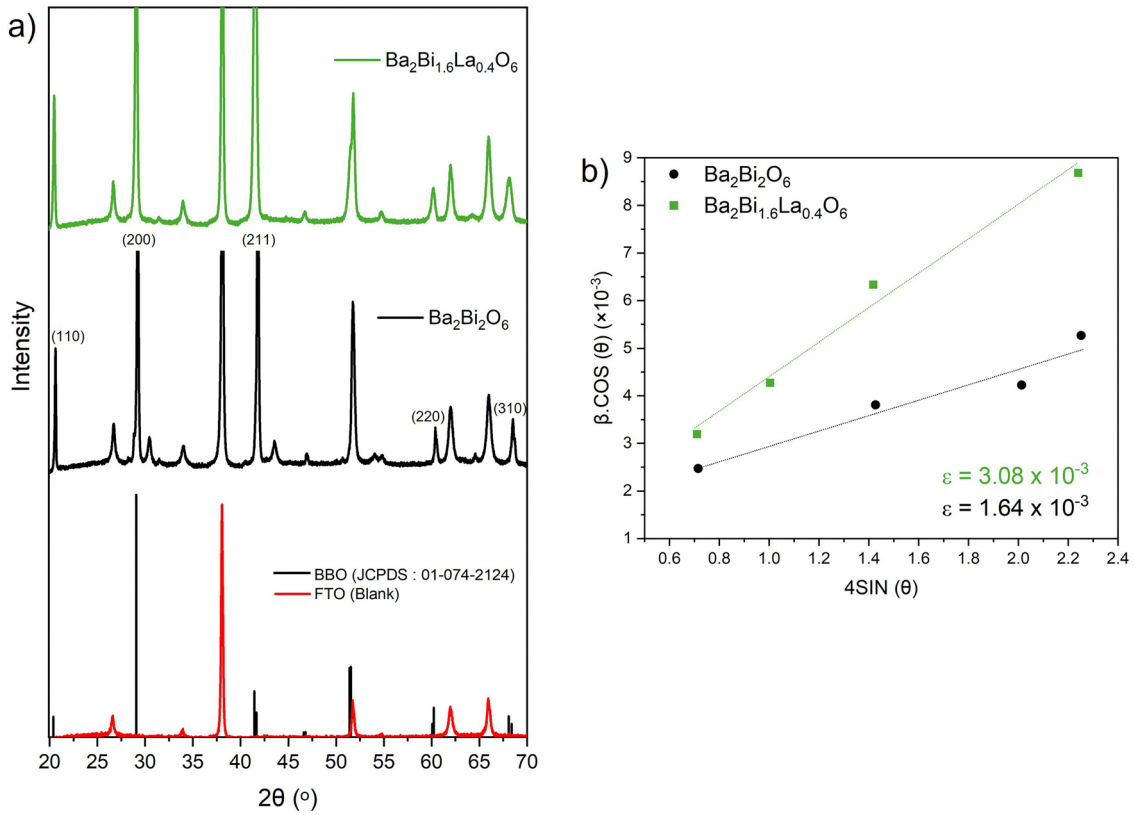

Fig. 3 (a) XRD diffractograms of $Ba_2Bi_{1.6}La_{0.4}O_6$ and $Ba_2Bi_2O_6$ films with reference to $Ba_2Bi_2O_6$ standard JCPDS 01-074-2124 and a blank FTO-glass substrate. (b) Williamson Hall plot using XRD diffractogram data of $Ba_2Bi_{1.6}La_{0.4}O_6$ and $Ba_2Bi_2O_6$ to calculate microstrain (ε).

suggesting that La substitution modifies the chemical environment and the resulting crystalline composition. The presence of this secondary subcarbonate phase only in the $Ba_2Bi_2O_6$ sample may also contribute to its inferior photocurrent performance.

Further quantitative analysis of the diffractograms using Williamson–Hall plots (eqn (3) in Experimental) was performed to calculate their microstrain (Fig. 3b). The microstrain for $Ba_2Bi_{1.6}La_{0.4}O_6$ (3.08×10^{-3}) is found to be nearly twice that of $Ba_2Bi_2O_6$ (1.64×10^{-3}), indicating increased lattice distortion, dislocations, and/or defects caused by internal stress from La substitution, which is also reported in other doped metal oxides.[30–32] This microstrain analysis provides a foundation for the computational findings and bandgap reduction later described.

To further investigate the microstructure and crystallinity of the films, high-resolution HAADF–STEM analysis was performed (Fig. 4). Low-magnification images reveal a continuous and conformal $Ba_2Bi_{1.6}La_{0.4}O_6$ film deposited on the FTO/glass substrate, with well-defined interfaces and no evidence of large-scale delamination, consistent with the FE-SEM images. The cross-sectional morphology confirms uniform coverage of the film over the substrate, with high porosity. High-magnification HAADF–STEM images (Fig. 4b–c) and corresponding Fourier transforms show the expected atomic arrangement viewed along the [220] zone axis, and are consistent with the distorted perovskite structure identified by XRD (JCPDS 01-074-2124). Crystallographic overlays, based on the monoclinic $I2/m$ $Ba_{1-x}k_xBiO_3$-type structure (COD ID: 1541112), agree with the experimental images. STEM–EDX elemental mapping (Fig. 4d) demonstrates a homogeneous spatial distribution of Ba, Bi, La, and O throughout the film thickness, confirming the successful incorporation of La into the lattice without any evidence of local phase segregation. The sharp interface between the $Ba_2Bi_{1.6}La_{0.4}O_6$ film layer and the Sn-containing FTO underlayer is also clearly resolved, indicating good interfacial integrity. Overall, the STEM analysis provides direct evidence of the high crystallinity and nanoscale compositional uniformity in the La-substituted films, complementing the FE-SEM and XRD results.

The incident photon-to-current efficiencies (IPCEs) at different wavelengths were measured at +1.05 V_{RHE}, at which dark currents were minimal. At 350 nm and +1.05 V_{RHE}, the IPCE is 2.20% for $Ba_2Bi_{1.6}La_{0.4}O_6$ and 1.25% for $Ba_2Bi_2O_6$ (Fig. 5a). This indicates a nearly two-fold boost in IPCE for La substitution at 20 at%. More interestingly, Tauc plots constructed with the IPCE spectra show a clear reduction in bandgap, from 2.70 eV for $Ba_2Bi_2O_6$ to 2.53 eV for $Ba_2Bi_{1.6}La_{0.4}O_6$. The decreased bandgap through La substitution enhances absorption of visible light within the film,[33–35] which likely contributes to the improvement in PEC activity.

To gain a deeper understanding of the effect La substitution has on improving photocurrent response, electrochemical

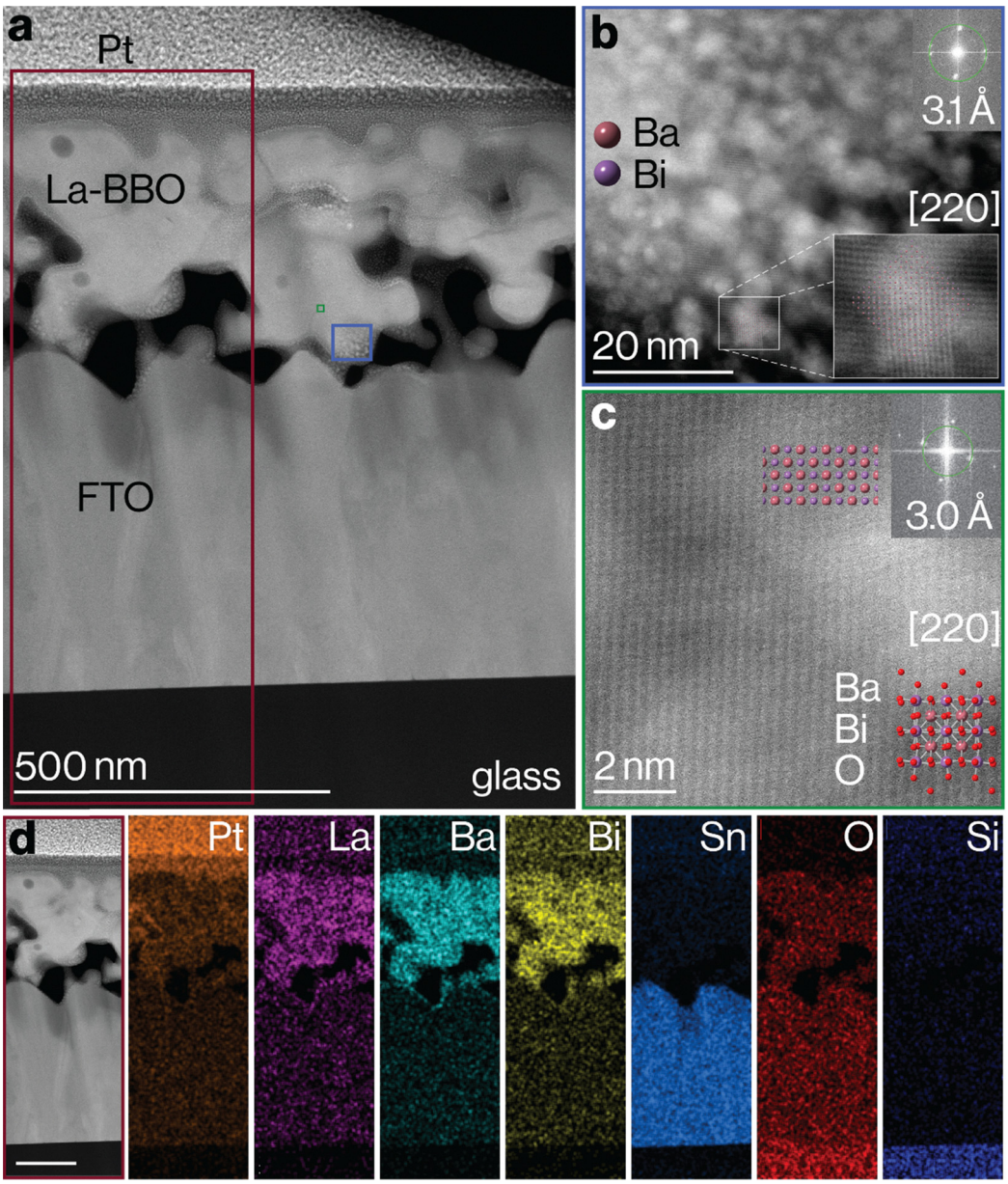

Fig. 4 (a) Low-magnification HAADF STEM image showing morphology of $Ba_2Bi_{1.6}La_{0.4}O_6$ on FTO film, with the Pt layer at the top deposited during FIB-SEM sample preparation. (b) and (c) High-magnification HAADF STEM images corresponding with the blue and green squares highlighted in (a). Corresponding Fourier transforms (inset in the top right corner of each image) and atomic overlays show a good match to the expected atomic structure of the monoclinic, *I*2/*m*, $Ba_{1-x}k_xBiO_3$ distorted perovskite structure (COD ID: 1541112, consistent with XRD results JCPDS 01-074-2124). Whilst atomic overlays exclude oxygen atoms for improved visibility, the full unit cell is inset in the bottom right of (c), where oxygen locally distorts the coordination around bismuth. (d) HAADF STEM image, corresponding with the red rectangle highlighted in (a), and accompanying STEM-EDS elemental maps (left to right) showing Pt, La, Ba, Bi, Sn, O and Si, accordingly. Scale bar in (d) is 200 nm. The Pt particles visible in (b) are an artefact of FIB sample preparation, arising from redeposition of the Pt protective layer.

impedance spectroscopy (EIS) and Mott–Schottky analysis were conducted. Although Mott–Schottky analysis is strictly applicable to nonporous planar films, the perovskite films investigated in this study are porous and nanostructured. Therefore, the extracted quantitative values should be interpreted with caution, but comparative analysis between samples remains meaningful. Mott–Schottky plots were derived from the EIS data to estimate charge-carrier densities (Fig. 5b–d). $Ba_2Bi_2O_6$ shows a flat response across the potential region ranges +1.4 to +1.0 V_{RHE} suggesting low conductivity for this material and explains the poor photocurrent performance. It is reported that a high density of surface states such as defects, acting as charge traps, can dominate the capacitance response, often leading to voltage-independent behaviour.[36,37] $Ba_2Bi_{1.6}La_{0.4}O_6$ has characteristic Mott–Schottky plots at all frequencies in which N_D values could be calculated through analysing the plot gradients.

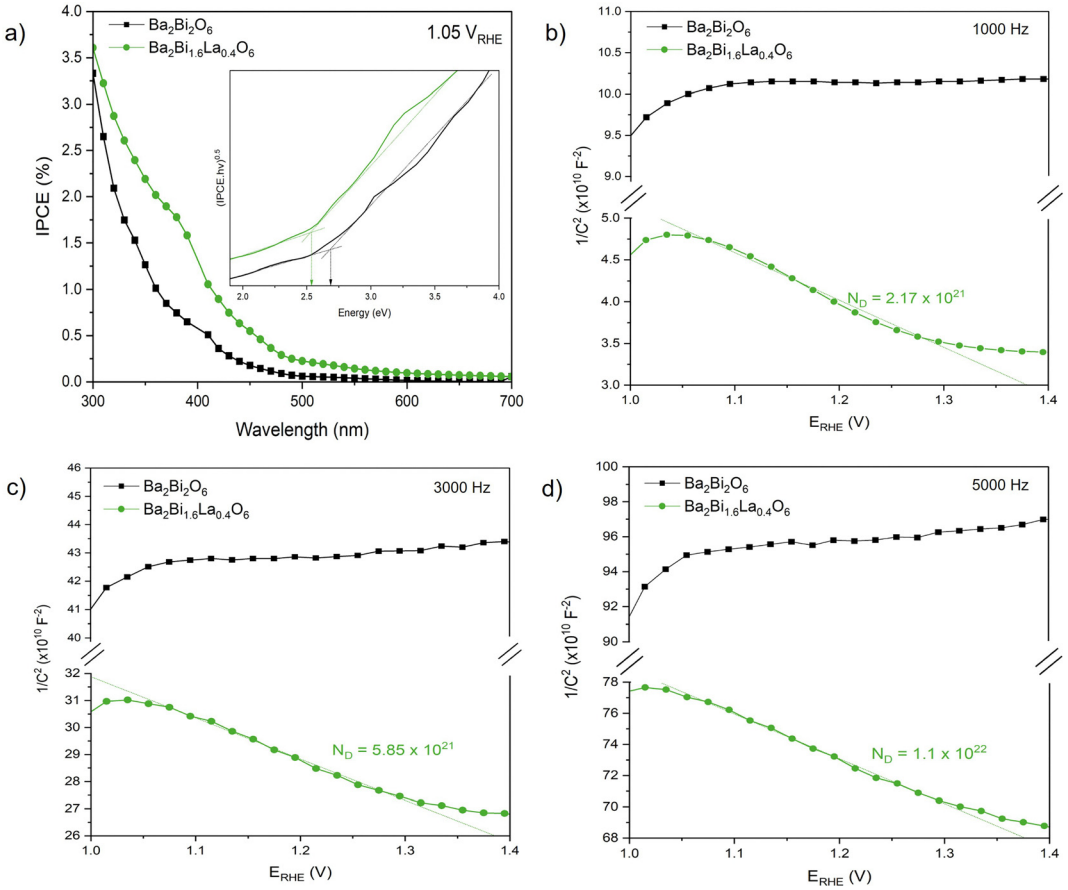

Fig. 5 (a) IPCE measurements for $Ba_2Bi_{1.6}La_{0.4}O_6$ and $Ba_2Bi_2O_6$ at +1.05 V_{RHE}. Mott Schottky plots for $Ba_2Bi_{1.6}La_{0.4}O_6$ and $Ba_2Bi_2O_6$, at (b) 1000 Hz, (c) 3000 Hz, and (d) 5000 Hz.

Therefore, La substitution has increased charge-carrier densities and enhanced material conductivity.[38–40] Although additional electrical measurements would be valuable in future studies on stabilised systems not affected by porosity and bismuth redox processes, this charge-carrier density effect, combined with improved light absorption, is proposed as an additional contributing factor to the enhanced photocurrent response in $Ba_2Bi_{1.6}La_{0.4}O_6$.

To deepen the understanding of both materials semiconducting behaviours, an energy band diagram was constructed using the bandgap values calculated using the IPCE Tauc plots (Fig. 5a) and data collected from Kelvin probe measurements and ambient photoelectron spectroscopy (APS) measuring the Fermi energy level and the valence band maximum (VBM), respectively (Fig. 6). Notable observations include the p-type character, beneficial for photocathodic reactions such as HER, as the Fermi energy level is closer in value to that of the VBM (Fig. 6a), and this p-type character is kept in the $Ba_2Bi_{1.6}La_{0.4}O_6$ samples. Secondly, the conduction band minimum (CBM) obtained by adding the measured bandgap from IPCE to the VBM is deeper in $Ba_2Bi_{1.6}La_{0.4}O_6$ than in $Ba_2Bi_2O_6$ (Fig. 6d). The CBM positions are estimated at approximately −3.01 eV for $Ba_2Bi_2O_6$ and −3.39 eV for $Ba_2Bi_{1.6}La_{0.4}O_6$ (*vs.* vacuum). At pH 12, the HER equilibrium potential is located at approximately −3.73 eV *vs.* vacuum, resulting in an energetic offset of ∼0.72 eV for $Ba_2Bi_2O_6$ and ∼0.34 eV for $Ba_2Bi_{1.6}La_{0.4}O_6$. Although the electron transfer to water remains thermodynamically feasible in both materials, this diminished driving force, combined with the presence of competing Bi redox processes, likely contributes to the lack of detectable hydrogen generation despite the observed photocurrents. Thirdly, a deeper VBM in $Ba_2Bi_{1.6}La_{0.4}O_6$ is observed by APS, 230 meV deepened upon La substitution (−5.712 eV *vs.* −5.942 eV, Fig. 6b).

Moreover, a significant difference in the integrated area below the photoemission threshold is observed in the APS spectra of both samples (Fig. 6b). Larger area in the region with lower energy than the VBM of $Ba_2Bi_2O_6$ implies a greater amount of mid-gap states near the VBM. This analysis provides direct evidence of defect-related electronic states, as sub-bandgap spectral weight in APS can be associated with trap states within the bandgap. To confirm the presence of mid-gap states, the surface photovoltage (SPV) of the samples was measured (Fig. 6c). For samples without underlying charge transport layers, like these ones, the influence of mid-gap states becomes significant. The positive signal of $Ba_2Bi_2O_6$ indicates an electron accumulation at the surface, suggesting that photogenerated electrons are being trapped at surface defects while the photogenerated charges in $Ba_2Bi_{1.6}La_{0.4}O_6$ directly recombine.

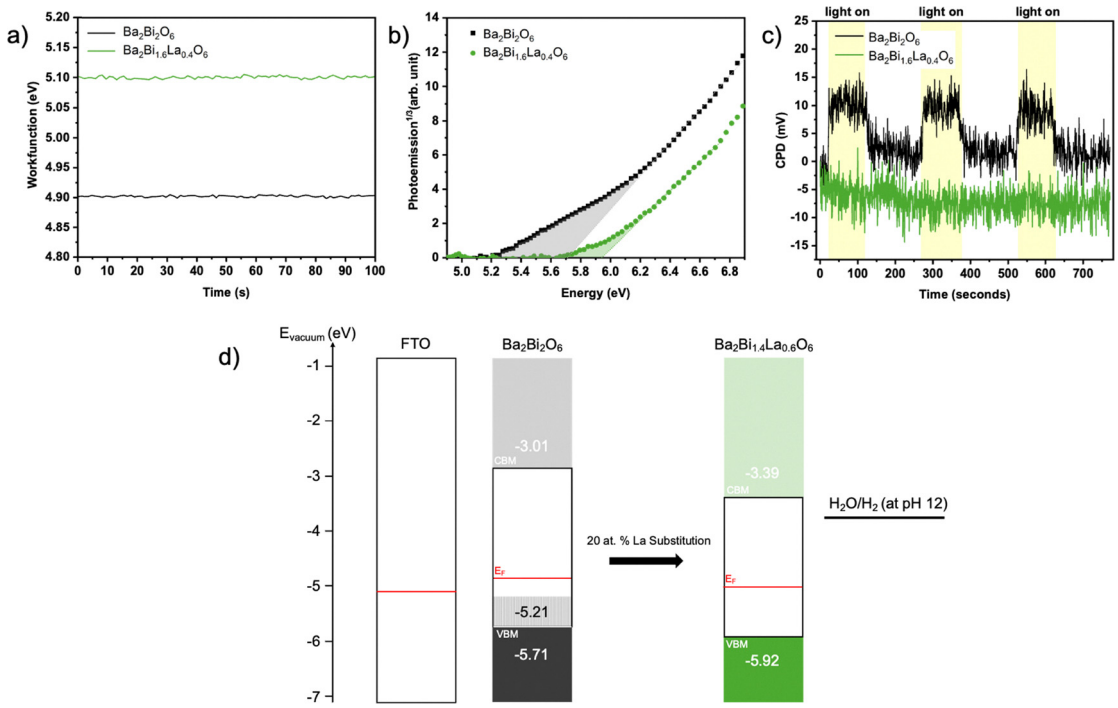

Fig. 6 (a) Work function values of $Ba_2Bi_2O_6$ and $Ba_2Bi_{1.6}La_{0.4}O_6$. (b) APS spectra of $Ba_2Bi_2O_6$ and $Ba_2Bi_{1.6}La_{0.4}O_6$. (c) Surface photovoltage (SPV) response of $Ba_2Bi_2O_6$ and $Ba_2Bi_{1.6}La_{0.4}O_6$ under 0.28 sun. (d) Band diagrams for $Ba_2Bi_2O_6$ and $Ba_2Bi_{1.6}La_{0.4}O_6$ with respect to the hydrogen evolution reaction at operating condition pH 12.

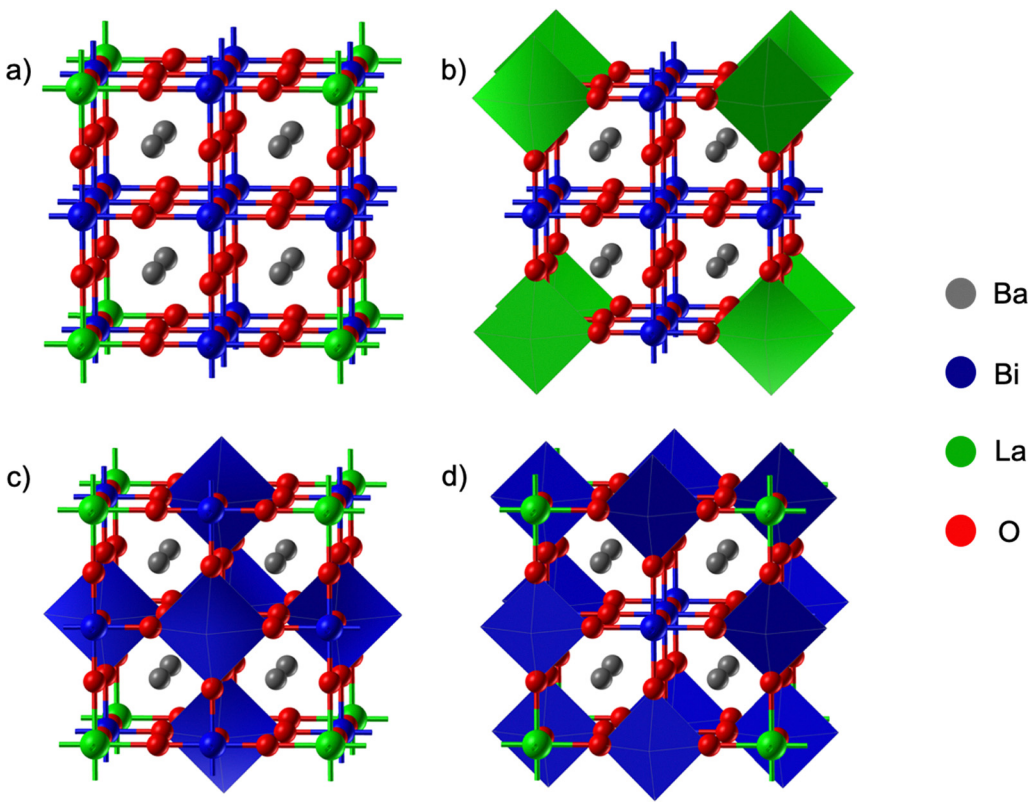

Fig. 7 (a) Geometric structure of the unit cell of $Ba_2Bi_{1.6}La_{0.4}O_6$. (b) larger La octahedra sites highlighted. (c)/(d) intermediate and small Bi octahedra sites highlighted.

The decreased SPV of $Ba_2Bi_{1.6}La_{0.4}O_6$ compared to $Ba_2Bi_2O_6$ illustrates that La substitution reduces trap states and thus surface band bending. Together, APS and SPV consistently indicate that La substitution reduces the density of defect/trap states, which contributes to improved charge transport and enhanced photocurrent performance.

The structural and electronic properties have been investigated using density functional theory, with the well documented global hybrid exchange functional, B3LYP, as implemented in the CRYSTAL23 code.[41,42] The local Gaussian basis sets used and numerical tolerances are provided in the SI. The structure of the $Ba_2Bi_{1.6}La_{0.4}O_6$ double perovskite is shown in Fig. 7a. It is evident that the positions of the oxygen atoms are not perfectly in the centre between Bi atoms and between La and Bi. There are three types of octahedra: larger ones with La–O distances of 2.33 Å (Fig. 7b), an intermediate type with Bi–O distances of 2.27 Å (Fig. 7c) and smaller octahetra with Bi–O distances of 2.10 Å (Fig. 7d). Beside the La^{3+} oxidation state, these values of Bi–O distances can be explained by considering the multiple oxidation states of Bi, which are Bi^{3+} and Bi^{5+} respectively, in a simple ionic model.

The density of states has been plotted to compare $Ba_2Bi_2O_6$ and $Ba_2Bi_{1.6}La_{0.4}O_6$ (Fig. 8). The zero value of the energy axes corresponds to the top of the valence band, which is made up of mainly oxygen 2p states with some addition from both Bi^{3+} (in blue) and Bi^{5+} (in cyan); the former contributes the most at the top of the valence band. Upon La substitution, the La states mix with the whole, mainly O 2p states, valence band. At the bottom of the conduction band, the Bi states dominate over the oxygen states in both systems. In the La-substituted material, La contributes negligibly to the conduction band.

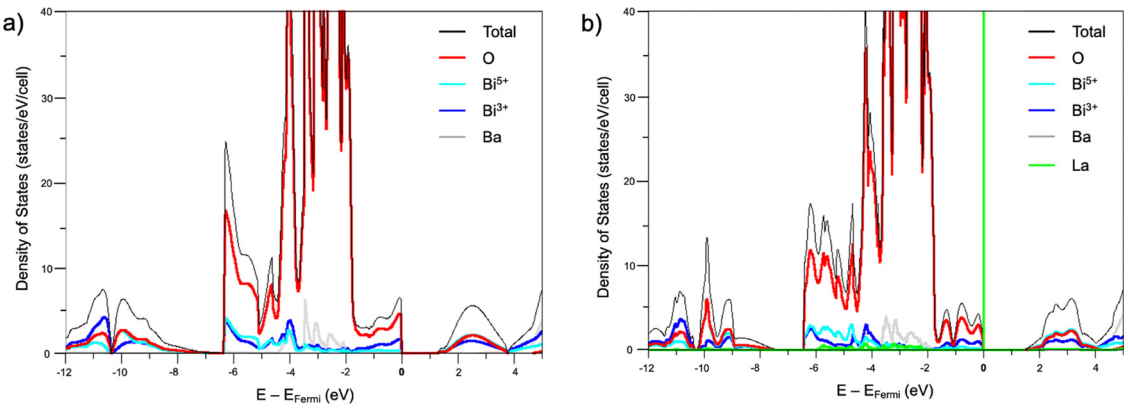

Fig. 8 Density of states plots for (a) $Ba_2Bi_2O_6$ and (b) $Ba_2Bi_{1.6}La_{0.4}O_6$ materials.

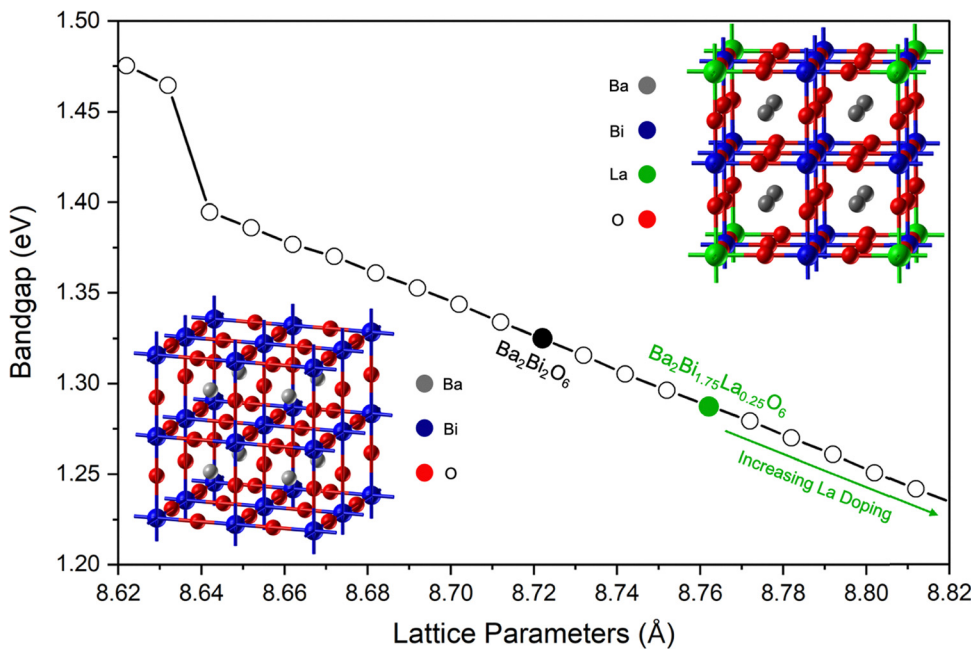

Fig. 9 Computed bandgap as a function of lattice parameter.

However, when substituting Bi with La, the lattice parameter increases, highlighted at the 12.5% concentration level the percentage of expansion is ~0.5%. The plot of the bandgap as a function of the lattice parameters is given in Fig. 9. When the lattice parameter increases (*i.e.* the system is strained), the band gap decreases. The bandgap is indirect for both samples. The calculated value is 1.33 eV for $Ba_2Bi_2O_6$. Entropically, La can occupy either Bi^{3+} or a Bi^{5+} sites; this affects the volume of the octahedra, as described previously in terms of Bi–O and La–O distances. This causes a frustration in the structure, since there is an expansion of all the La-octahedra. When this happens, there is a strong reduction of the bandgap, which is absent when only one type of Bi-octahedra is affected, evident from the density of states reported above for an ordered system with La.

Altogether, the data presented here demonstrate the combined benefits of using a polymer templating approach for fabricating La-substituted $Ba_2Bi_{1.6}La_{0.4}O_6$ and $Ba_2Bi_2O_6$ thin films, highlighting the resulting effects on their structural, electronic, and PEC properties. Incorporation of the PVP template facilitated the formation of uniform films with desirable porosity and well-defined grain boundaries, as evidenced by SEM and STEM, thereby improving interfacial semiconductor contact with the electrolyte. La substitution at 20 at% is found to activate conductivity, as evidenced by the transition from a flat, for $Ba_2Bi_2O_6$, to positively sloped Mott–Schottky response for $Ba_2Bi_{1.6}La_{0.4}O_6$. Simultaneously, XRD analysis applying the Williamson–Hall equation indicates an increase in microstrain within the crystal lattice upon La substitution. This finding is further supported by computational simulations and illustrated by a plot of bandgap *versus* lattice parameters, which show that as the lattice parameters, and thus strain, increases, the bandgap decreases. The induced strain corresponded to a noticeable reduction in the optical bandgap, which drops from 2.70 to 2.53 eV, as determined from Tauc plots based on IPCE measurements. Collectively, these modifications yield enhanced photocurrent response, with the optimal composition $Ba_2Bi_{1.6}La_{0.4}O_6$ achieving a peak photocurrent density of –0.85 mA cm^{-2} at +0.68 V_{RHE}. Nevertheless, no hydrogen gas can be detected; therefore, the origin of the photocurrent is attributed primarily to the redox activity of bismuth species, indicating a critical limitation in their application for selective PEC reduction reactions. These findings underscore the necessity for further development of these materials to leverage their properties in photocathodic reactions in aqueous electrolytes.

Conclusion

Thin films of the double perovskite $Ba_2Bi_2O_6$, both without and with 20% La atomic substitution for Bi ($Ba_2Bi_{1.6}La_{0.4}O_6$), have been successfully fabricated on transparent conductive substrates, using spin coating of a sol–gel mixture incorporating a polyvinylpyrrolidone polymer template. Scanning electron micrographs show that the beneficial effect of incorporating the polymer template, producing uniform films with distinct grain boundaries and good levels of porosity to maximise semiconductor–electrolyte interactions. Mott–Schottky plots reveals measurable charge carrier concentrations for $Ba_2Bi_{1.6}La_{0.4}O_6$, obtained from the slope of the plot, whereas $Ba_2Bi_2O_6$ exhibits a flat response. This indicates that La substitution activates conductivity, improving charge transport in the film. Tauc plots, calculated from the incident photon-to-current efficiencies (IPCE) measured at +1.05 V_{RHE}, show a clear bandgap reduction upon La substitution, from 2.7 to 2.53 eV. This smaller bandgap further contributes to the improved performance of $Ba_2Bi_{1.6}La_{0.4}O_6$, by enabling stronger light absorption. X-ray diffractograms confirms that samples are crystalline, and Williamson–Hall analysis shows that La substitution doubles the microstrain, a result supported by computational modelling. High-resolution HAADF–STEM and elemental mapping further confirms the crystallinity, interfacial integrity, and nanoscale compositional uniformity of the La-substituted films. The calculations also indicate that La substitution expands the lattice parameters and introduces microstrain, which reduces the bandgap in a nearly linear manner, explaining the observed optical change. Photoelectrochemical measurements show that $Ba_2Bi_{1.6}La_{0.4}O_6$ achieves a maximum photocurrent density of −0.85 mA cm^{-2} at +0.68 V_{RHE}. However, these currents are not confirmed to arise from hydrogen evolution and are instead attributed to the reduction of bismuth through its various oxidation states. Overall, these results demonstrate the potential to achieve high photocurrents in La-modified $Ba_2Bi_2O_6$ while also highlighting the remaining challenge of directing these photocurrents toward practical reactions such as hydrogen generation.

Conflicts of interest

The authors have no conflicts of interest to declare.

Data availability

The data that support the findings of this study are openly available in the following Figshare data repository at https://doi.org/10.6084/m9.figshare.32287107. Supplementary information including current–potential curves, photographs, XPS spectra and computational tables. See DOI: https://doi.org/10.1039/d5ma01435b.

Acknowledgements

This work was supported and funded by bp – International Centre for Advanced Materials (bp-ICAM) on project ICAM-82 (Novel Photocathodes for Hydrogen Production) and the Engineering and Physical Sciences Research Council (EPSRC) through the CDT in Advanced Characterisation of Materials (EP/S515085/1). We would like to acknowledge both for their financial support. S.E. acknowledges the funding of the UK Engineering and Physical Sciences Research Council (EPSRC) provided *via* grant EP/S030727/1. TEM access was supported by the Henry Royce Institute for Advanced Materials, funded

through EPSRC grants EP/R00661X/1, EP/S019367/1, EP/P025021/1, and EP/P025498/1. S.J.H. and E.T acknowledge funding from the EPSRC under grants EP/Y024303/1 and EP/V001914/1. JSK thanks the Ewha Global Excellence Program.

References

1 P. Periasamy and Y. K. Mohanta, *Green Nanomaterials in Energy Conversion and Storage Applications*, 2024, New York, pp. 45–73.

2 Fossil fuels and the state of the energy crisis: WWF, https://wwf.panda.org/wwf_news, (accessed 25 March 2025).

3 P. Achakulwisut, P. Erickson, C. Guivarch, R. Schaeffer, E. Brutschin and S. Pye, Global fossil fuel reduction pathways under different climate mitigation strategies and ambitions, *Nat. Commun.*, 2023, **14**, 1–15.

4 Renewable energy – powering a safer future: United Nations, https://www.un.org/en/climatechange/raising-ambition/renewable-energy, (accessed 25 March 2025).

5 G. Rothenberg, A realistic look at CO_2 emissions, climate change and the role of sustainable chemistry, *Sustain. Chem. Clim. Action*, 2023, **2**, 100012.

6 P. Stegmann, V. Daioglou, M. Londo, D. P. van Vuuren and M. Junginger, Plastic futures and their CO_2 emissions, *Nature*, 2022, **612**, 272–276.

7 M. El ouardi, A. El Idrissi, M. Arab, M. Zbair, H. Haspel, M. Saadi and H. Ait Ahsaine, Review of photoelectrochemical water splitting: From quantitative approaches to effect of sacrificial agents, oxygen vacancies, thermal and magnetic field on (photo)electrolysis, *Int. J. Hydrogen Energy*, 2024, **51**, 1044–1067.

8 J. M. Yu, J. Lee, Y. S. Kim, J. Song, J. Oh, S. M. Lee, M. Jeong, Y. Kim, J. H. Kwak, S. Cho, C. Yang and J. W. Jang, High-performance and stable photoelectrochemical water splitting cell with organic-photoactive-layer-based photoanode, *Nat. Commun.*, 2020, **11**, 1–9.

9 A. Ziani, I. Al-Shankiti, M. A. Khan and H. Idriss, Demonstration of green hydrogen production using solar energy at 28% efficiency and evaluation of its economic viability, *Sustainable Energy Fuels*, 2020, **34**, 13179–13185.

10 I. Roger, M. A. Shipman and M. D. Symes, Earth-abundant catalysts for electrochemical and photoelectrochemical water splitting. Nature Reviews, *Chemistry*, 2017, **1**, 1–13.

11 A. Odenweller and F. Ueckerdt, The green hydrogen ambition and implementation gap, *Nat. Energy*, 2025, **10**, 110–123.

12 Z.-Y. Yu, Y. Duan, X.-Y. Feng, X. Yu, M.-R. Gao, S.-H. Yu, Z. Yu, Y. Duan, X. Feng, X. Yu, M. Gao and S. Yu, Clean and Affordable Hydrogen Fuel from Alkaline Water Splitting: Past, Recent Progress, and Future Prospects, *Adv. Mater.*, 2021, **33**, 2007100.

13 W. Yang and J. Moon, Recent Advances in Earth-Abundant Photocathodes for Photoelectrochemical Water Splitting, *ChemSusChem*, 2019, **12**, 1889–1899.

14 T. Yao, X. An, H. Han, J. Q. Chen and C. Li, Photoelectrocatalytic Materials for Solar Water Splitting. Advanced Energy, *Materials*, 2018, **8**, 1800210.

15 C. Li, J. He, Y. Xiao, Y. Li and J. J. Delaunay, Earth-abundant Cu-based metal oxide photocathodes for photoelectrochemical water splitting, *Energy Environ. Sci.*, 2020, **13**, 3269–3306.

16 M. I. Díez-García and R. Gómez, Progress in Ternary Metal Oxides as Photocathodes for Water Splitting Cells: Optimization Strategies, *Solar RRL*, 2022, **6**, 2100871.

17 E. Freeman, S. Kumar, V. Celorrio, M. S. Park, J. H. Kim, D. J. Fermin and S. Eslava, Strategies for the deposition of LaFeO3 photocathodes: improving the photocurrent with a polymer template, *Sustainable Energy Fuels*, 2020, **4**, 884–894.

18 M. Schleuning, M. Kölbach, I. Ahmet, R. Präg and R. Gottesman, *et al.*, Carrier Localization on the Nanometer-Scale limits Transport in Metal Oxide Photoabsorbers, *Adv. Funct. Mater.*, 2023, **33**, 2300065.

19 G. Hodes and P. V. Kamat, Understanding the Implication of Carrier Diffusion Length in Photovoltaic Cells, *J. Phys. Chem. Lett.*, 2015, **6**, 4090–4092.

20 H. J. Ahn, M. J. Kwak, J. S. Lee, K. Y. Yoon and J. H. Jang, Nanoporous hematite structures to overcome short diffusion lengths in water splitting, *J. Mater. Chem. A*, 2014, **2**, 19999–20003.

21 E. Freeman, S. Kumar, S. R. Thomas, H. Pickering, D. J. Fermin and S. Eslava, $PrFeO_3$ Photocathodes Prepared Through Spray Pyrolysis, *ChemElectroChem*, 2020, **7**, 1365–1372.

22 A. Banerjee, M. K. Awasthi, P. Maji, M. Pal, S. T. Aziz, G. K. Lahiri and A. Dutta, Double Perovskite Oxides Bringing a Revelation in Oxygen Evolution Reaction Electrocatalyst Design, *ChemElectroChem*, 2023, **10**, e202201098.

23 N. I. Kim, S. H. Cho, S. H. Park, Y. J. Lee, R. A. Afzal, J. Yoo, Y. S. Seo, Y. J. Lee and J. Y. Park, B-site doping effects of $NdBa_{0.75}Ca_{0.25}Co_2O_{5+\delta}$ double perovskite catalysts for oxygen evolution and reduction reactions, *J. Mater. Chem. A*, 2018, **6**, 17807–17818.

24 T. Guo, W. T. Fu and H. J. M. de Groot, Engineering $Ba_2Bi_2O_6$ Double Perovskite with La^{3+} for High Current Density Visible Light Photoelectrochemical Hydrogen Evolution, *Small*, 2024, **20**, 2308781.

25 J. Shi, E. A. Rubinstein, W. Li, J. Zhang, Y. Yang, T. L. Lee, C. Qin, P. Yan, J. L. MacManus-Driscoll, D. O. Scanlon and K. H. L. Zhang, Modulation of the Bi^{3+} $6s^2$ Lone Pair State in Perovskites for High-Mobility p-Type Oxide Semiconductors. Advanced, *Science*, 2022, **9**, 2104141.

26 B. Weng, C. R. Grice, J. Ge, T. Poudel, X. Deng and Y. Yan, Barium Bismuth Niobate Double Perovskite/Tungsten Oxide Nanosheet Photoanode for High-Performance Photoelectrochemical Water Splitting. Advanced Energy, *Materials*, 2018, **8**, 1701655.

27 V. Vivier, A. Régis, G. Sagon, J. Y. Nedelec, L. T. Yu and C. Cachet-Vivier, Cyclic voltammetry study of bismuth oxide Bi_2O_3 powder by means of a cavity microelectrode coupled with Raman microspectrometry, *Electrochim. Acta*, 2001, **46**, 907–914.

28 G. Milazzo and S. Caroli, *Tables of Standard Electrode Potentials*, Wiley, New York, 1978.

29 B. F. Lewis, C. Huang, I. Itskou, G. Mallia, N. M. Harrison, J. Southouse and S. Eslava, Ca-Doped $PrFeO_3$ Photocathodes with Enhanced Photoelectrochemical Activity, *Solar RRL*, 2024, **8**, 2400308.
30 S. Siyalo, H. F. Etefa and F. B. Dejene, Enhancing Structural and Optical Properties of CuO Thin Films through Gallium Doping: A Pathway to Enhanced Photoluminescence and Predict for Solar Cells Applications, *Chem. Phys. Impact*, 2025, **10**, 100832.
31 C. Mrabet, M. Ben Amor, A. Boukhachem, M. Amlouk and T. Manoubi, Physical properties of La-doped NiO sprayed thin films for optoelectronic and sensor applications, *Ceram. Int.*, 2016, **42**, 5963–5978.
32 N. Khlifi, S. Mnif, F. Ben Nasr, N. Fourati, C. Zerrouki, M. M. Chehimi, H. Guermazi, S. Aifa and S. Guermazi, Non-doped and transition metal-doped CuO nano-powders: structure-physical properties and anti-adhesion activity relationship, *RSC Adv.*, 2022, **12**, 23527–23543.
33 P. Riente and T. Noël, Application of metal oxide semiconductors in light-driven organic transformations, *Catal. Sci. Technol.*, 2019, **9**, 5186.
34 W. S. Choi, M. F. Chisholm, D. J. Singh, T. Choi, G. E. Jellison and H. N. Lee, Wide bandgap tunability in complex transition metal oxides by site-specific substitution, *Nat. Commun.*, 2012, **3**, 1–6.
35 M. H. Miah, M. U. Khandaker, M. B. Rahman, M. Nur-E-Alam and M. A. Islam, Band gap tuning of perovskite solar cells for enhancing the efficiency and stability: issues and prospects, *RSC Adv.*, 2024, **14**, 15876–15906.
36 S. M. Sze and K. K. Ng, *Physics of Semiconductor Devices*, Wiley, New York, 2006.
37 C. R. Crowell and G. I. Roberts, Surface State and Interface Effects on the Capacitance-Voltage Relationship in Schottky Barriers, *J. Appl. Phys.*, 1969, **40**, 3726–3730.
38 J. Euvrard, Y. Yan and D. B. Mitzi, Electrical doping in halide perovskites, *Nat. Rev. Mater.*, 2021, **6**, 531–549.
39 M. S. Hammer, D. Rauh, V. Lorrmann, C. Deibel and V. Dyakonov, Effect of doping- and field-induced charge carrier density on the electron transport in nanocrystalline ZnO, *Nanotechnology*, 2008, **19**, 485701.
40 J. S. Park, S. Kim, Z. Xie and A. Walsh, Point defect engineering in thin-film solar cells, *Nat. Rev. Mater.*, 2018, **3**, 194–210.
41 A. Erba, J. K. Desmarais, S. Casassa, B. Civalleri, L. Donà, I. J. Bush, B. Searle, L. Maschio, L. Edith-Daga, A. Cossard, C. Ribaldone, E. Ascrizzi, N. L. Marana, J. P. Flament and B. Kirtman, CRYSTAL23: A Program for Computational Solid State Physics and Chemistry, *J. Chem. Theory Comput.*, 2023, **19**, 6891–6932.
42 R. Dovesi, V. R. Saunders, C. Roetti, R. Orlando, C. M. Zicovich-Wilson, F. Pascale, B. Civalleri, K. Doll, N. M. Harrison, I. J. Bush, Ph D'Arco, M. Llunell, M. Causà, Y. No&eul, L. Maschio, A. Erba, M. Rerat, S. Casassa, B. G. Searle and J. K. Desmarais, *CRYSTAL23 User's Manual*, Torino, 2023.